



An intrinsic descriptor of perovskite cobaltites for catalytic peroxyomonosulfate activation toward water remediation

Kai Wang^{a,b}, Chen Han^b, Fuping Li^b, Yu Liu^b, Zongping Shao^{b,*}, Lihong Liu^b, Shaobin Wang^{c,*}, Shaomin Liu^{a,b,**}

^a State Key Laboratory of Organic-Inorganic Composites, College of Chemical Engineering, Beijing University of Chemical Technology, Beijing 100029 China

^b WA School of Mines: Minerals, Energy and Chemical Engineering, Curtin University, Perth, WA 6102 Australia

^c School of Chemical Engineering and Advanced Materials, The University of Adelaide, Adelaide, SA 5005, Australia

ARTICLE INFO

Keywords:

Perovskite oxide
Mechanism
Crystal structure
Advanced oxidation processes,
Peroxyomonosulfate

ABSTRACT

A series of strontium cobaltite perovskite oxides with various dopants ($\text{SrCo}_{0.95}\text{M}_{0.05}\text{O}_{3-\delta}$, $\text{M}=\text{Fe, Sc, Co, Zn, Gd}$) are designed for catalytic peroxyomonosulfate (PMS) activation to degrade aqueous organic pollutants and the correlations between their crystalline structure and surface properties to catalytic activity were comprehensively investigated. $\text{SrCo}_{0.95}\text{M}_{0.05}\text{O}_{3-\delta}$ displays three crystalline structures depending on the dopant metals and exhibits different catalytic activities. Among the structures and properties, Co-O bond length significantly affects the lattice oxygen diffusivity and $\text{Co}^{2+}/\text{Co}^{3+}$ redox capacity, governing the overall PMS activation, and is suggested as a descriptor for PMS activation. This study provides new insight to the reaction pathways and the structure-activity correlation for new design of effective perovskite oxides for PMS-based oxidation process toward wastewater treatment and other catalytic processes.

1. Introduction

The increased water contamination and clean water scarcity have threatened public health and the ecosystem and restricted sustainable development worldwide. The fast global industrialization needs water supply much more than expected, thus has stimulated considerable research efforts towards the development of new technologies for wastewater treatment. Among them, peroxyomonosulfate (PMS)-based advanced oxidation processes (AOPs) manifest as a promising approach to generate highly reactive oxygen species (ROS) in-situ for oxidation of organic pollutants and mineralization [1–3]. In this oxidation system, an activator plays a vital role in catalytic PMS activation for ROS generation, and fundamental understanding of the process would help design a new catalytic system for the AOPs.

Perovskite oxides as an important category of functional materials have gained immense attentions in the area of oxygen reduction/evolution reaction (ORR, OER), hydrogen evolution, photocatalysis and water remediation [4–7]. The advantages of tunable composition and physicochemical properties, such as controllable electron structure and

defect density, endow perovskite oxides with unprecedented catalytic performance, which even outperforms the noble metals and their oxides. For instance, Shao-Horn's group proposed that e_g orbital occupancy of 3d transition metal (TM) on the surface of perovskite oxides governed the OER activity, where $\text{Ba}_{0.5}\text{Sr}_{0.5}\text{Co}_{0.8}\text{Fe}_{0.2}\text{O}_{3-\delta}$ (BSCF) with an e_g occupancy close to unity of surface TMs exhibited almost an order of magnitude higher catalytic OER performance than IrO_2 [8]. Similar findings were made by Su et al. [9] and Miao et al. [10] that the highest PMS activation efficiency over Co-based perovskite oxides ($\text{PrBaCo}_2\text{O}_{5+\delta}$ and LaCoO_3) can be attributed to the e_g occupancy close to unity of surface Co, where the adsorption between surface Co and PMS is moderate to promote PMS activation and ROS generation.

In addition to the effects from transitional metal cations, oxygen defects (oxygen vacancy and interstitial oxygen) are regarded as another type of important active sites for promoting the catalytic performance [11,12]. It has been reported that both surface oxygen vacancy (OV) and interstitial oxygen could directly activate PMS efficiently, mainly contributing to the singlet oxygen (${}^1\text{O}_2$) formation [13,14]. OV could easily transfer to active oxygen by depriving an oxygen from a PMS

* Corresponding authors.

** Corresponding author at: State Key Laboratory of Organic-Inorganic Composites, College of Chemical Engineering, Beijing University of Chemical Technology, Beijing 100029 China.

E-mail addresses: zongping.shao@curtin.edu.au (Z. Shao), shaobin.wang@adelaide.edu.au (S. Wang), liushaomin@mail.buct.edu.cn (S. Liu).

molecule and then couple with another PMS molecule to generate singlet oxygen, while the interstitial oxygen could directly decompose PMS to generate singlet oxygen for organics oxidation [15,16]. Of course, the participation of active oxygen in these redox reactions cannot be fulfilled without the aid of cation defects; thus defect engineering has been well developed to tailor the electronic feature by introducing the cation non-stoichiometry via aliovalent/isovalent doping or post-treatment [12,14,16].

In addition to the alterations of electronic configuration and defect structure, crystal phase of perovskite oxides is also a critical factor influencing catalytic activity. Zhou et al. reported that high temperature sintering could alter a rhombohedral crystal of $\text{LaNiO}_{3-\delta}$ to a cubic phase, thus resulting a larger Fermi surface on the cubic $\text{LaNiO}_{3-\delta}$ and enhancing both OER and ORR activities remarkably [17]. Besides, A-site doped $\text{La}_{1-x}\text{Sr}_x\text{FeO}_{3-\delta}$ with catalytically inert rare-earth element Sr was prepared and exhibited different crystal structures depending on the dopant content. For example, $\text{La}_{0.2}\text{Sr}_{0.8}\text{FeO}_{3-\delta}$ with a cubic phase not only showed the lowest overpotential but also presented superior stability for a long cycle test in comparison with other hexagonal and tetragonal structures [18]. Moreover, anion doping was also employed to stabilize cubic $\text{SrCoO}_{2.85-\delta}\text{F}_{0.15}$ to make it show higher density of surface reactive oxygen species, thus more effective for OER than pristine hexagonal $\text{SrCoO}_{3-\delta}$ [19]. The superiority of cubic structure was also verified in photocatalysis. Li and co-workers experimentally compared the catalytic activities of cubic and orthorhombic NaNbO_3 for photo reduction of CO_2 and H_2 evolution, and a two-fold enhancement of photocatalytic performance was observed for cubic structure compared to the orthorhombic one [20]. Theoretical analysis suggests that such an enhancement can be ascribed to the optimized electronic structure induced by the highly symmetric structure, favoring the excitation of photoelectrons and transfer.

As stated above, many factors of perovskites, such as oxygen defects, crystal structure, the e_g orbital occupancy of 3d transition metal cations on perovskite oxide surface, morphology, pore structure, and specific surface area, could jointly affect the catalytic activity of perovskite oxides. Understanding the main factors that largely determine the catalytic performance for PMS activation will greatly help optimize the catalysts from hundreds of potential compositions available. $\text{SrCoO}_{3-\delta}$ is an important parent perovskite oxide, from which various compositions can be derived with a wide range of oxygen non-stoichiometry and different phase structures for multiple applications [21,22], such as oxygen separation [23], solid oxide fuel cells [24], and OER/ORR [25]. Depending on the synthesis method, sintering temperature, doping elements and post-treatment, the phase of $\text{SrCoO}_{3-\delta}$ can be in hexagonal, oxygen vacancy ordered brownmillerite, rhombohedral or cubic structures [26–28]. Given the nature of easy transformation of crystal structure and high efficiency of Co-based oxides for PMS activation, the parent $\text{SrCoO}_{3-\delta}$ is an ideal model material for catalyst design.

In this work, a doping strategy on the B-site of $\text{SrCoO}_{3-\delta}$ by 5 mol% of a foreign element M (Fe, Sc, Zn, or Gd) to replace Co was applied to obtain a series of perovskites oxides of $\text{SrCo}_{0.95}\text{M}_{0.05}\text{O}_{3-\delta}$. The physico-chemical properties of these samples, such as phase structure, oxygen vacancy concentration, electron configuration, electronic conductivity were carefully investigated, and their catalytic activities in PMS activation were correlated with some measurable parameters, such as surface functional groups, oxygen vacancy, Co-O bond length, lattice oxygen diffusivity, and $\text{Co}^{2+}/\text{Co}^{3+}$ redox capability, to determine the. It was surprisingly found that PMS activation activity exhibited a direct correlation with the average Co-O bond length. The M-dopants induced a phase transition from pristine hexagonal to tetragonal and orthorhombic brownmillerite structures, gradually weakening the Co-O covalency and consequently leading to an elongated Co-O bond length. The elongated Co-O system favors the lattice oxygen diffusion activity, thus promoting more active $\text{Co}^{2+}/\text{Co}^{3+}$ redox reaction for PMS activation.

2. Experimental section

2.1. Catalyst syntheses

$\text{SrCo}_{0.95}\text{M}_{0.05}\text{O}_{3-\delta}$ (SrCoM , M=Fe, Sc, Co, Zn, Gd) perovskite oxides were synthesized via a sol-gel approach using ethylenediaminetetraacetic acid (EDTA) and citric acid as complexing reagents. Typically, stoichiometric amounts of metal nitrates were dissolved in ultrapure water (10 mL) obtained from a Millipore water system under successive agitation. EDTA and citric acid at required amounts were added into the nitrate salt solution according to the molar ratio of 1:1:2 for the total metal ions, EDTA, and citric acid. Ammonia solution was then employed to adjust the pH to ~6 to achieve a complete complexing and the obtained solution was stirred continuously at 80 °C until getting a transparent gel. Then two sintering steps were introduced to finalize the perovskite preparation. The transparent gel was heated at 190 °C for 10 h, followed by a high temperature pyrolysis step (1100 °C × 5 h).

2.2. Characterizations

The crystal structures of SrCoM powders were revealed by X-ray diffraction (XRD, Bruker D8) with filtered $\text{Cu K}\alpha$ radiation. The XRD spectra were recorded between the range of 10–90° (2θ) with an interval of 0.019°. The detailed structure information including space group and lattice parameters was obtained by Rietveld refinement analysis using Topas software. Nitrogen adsorption isotherms were performed on a Tristar II plus under –196 °C and the specific surface areas were calculated via the Brunauer-Emmett-Teller (BET) method. High resolution transmission electron microscopy (HR-TEM) images and energy-dispersive X-ray spectroscopy (EDS) results were obtained on a transmission electron microscope (TEM, FEI Titan G2 80–200) with an EDS analyzer at an accelerating voltage of 200 kV. The surface chemical properties were analyzed by X-ray photoelectron spectroscopy (XPS, Thermo ESCALAB 250) with an excitation source of $\text{Al-K}\alpha$ X-rays at a photon energy of 1486.7 eV. Identification of oxygen reactive species was performed on electron paramagnetic resonance (EPR, Bruker) using 5,5-dimethyl-1-pyrroline N-oxide (DMPO) and 2,2,6,6-tetramethylpyridine (TEMP) as trapping reagents. Fourier transform-infrared spectra were obtained by Fourier transform-infrared spectroscopy (FT-IR, Agilent). In-situ Raman spectra were collected on a WITEC alpha 300RA+. To obtain clear Raman signals, the concentrations of both PMS and catalyst have been increased by 100 times to those in the real reaction system.

2.3. Various electrochemical measurements

Electrochemical measurements including open circle potential (OCP), electrochemical impedance spectroscopy (EIS), cyclic voltammetry (CV) and linear sweep voltammetry (LSV) were carried out on an electrochemical workstation (Gamry, reference 3000). A glassy carbon electrode with a diameter of 5 mm coated with a SrCoM catalyst was used as the working electrode. In preparation of the electrode, a homogeneous catalyst ink was first prepared by mixing 10 mg catalyst, 10 mg black carbon and 100 μL Nafion (5 wt%, Sigma-Aldrich) within 1 mL absolute ethanol and sonicating for 30 min. Then 7 μL ink was transferred to the electrode and dry under room temperature. A platinum wire and an Ag/AgCl (4 M KCl) were used as counter electrode and reference electrode, respectively. CV curves were obtained with a scan rate of 50 mV/s. EIS tests were conducted from 10^5 to 10^{-1} Hz with an AC voltage of 5 mV at –0.3 V vs. Ag/AgCl . LSV was tested from 0.2 to 1.5 V vs. Ag/AgCl at a scan speed of 5 mV/s. A two-electrode system (working electrode and platinum electrode) was used for an open circle potential test. Before the test, the working electrode was immersed in 0.1 M Na_2SO_4 electrolyte for 24 h to achieve a stable overpotential.

2.4. Degradation of organics

A typical kinetic experiment was performed in a volume of 250 mL reactor under continuous stirring (300 rpm) at 25 °C by introducing an activator (SrCoM , 0.1 g L⁻¹) and PMS (0.5 g L⁻¹) into 200 mL of 4-hydroxybenzoic acid (HBA) solution (50 ppm). At a certain time interval, the solution samples were withdrawn and analyzed by ultra-high performance liquid chromatography (UHPLC, Thermo-Fisher) with a UV detector at the wavelength of 252 nm. A SB-C18 column (Agilent Poroshell 120) was used and the mobile phase containing 70% methanol and 30% formic acid (1 vol%) was run at 0.3 mL min⁻¹. The degradation efficiency of organics was calculated based on Eq. (1).

$$\text{Degradation efficiency} = \frac{C}{C_{\text{ads}}} \quad (1)$$

Where, the C and C_{ads} are the concentration of organics at time t (min) and concentration after achieving an adsorption/desorption equilibrium.

3. Results and discussion

3.1. Structural characterizations

Srontium cobaltite ($\text{SrCoO}_{3.8}$)-based materials can display several crystal structures, depending on various factors, such as preparation method, chemical compositions, and testing conditions in particular at high temperature, pressure and gas atmosphere. It has been

demonstrated that a phase transition sequence of $\text{SrCoO}_{3-\delta}$ from low to high symmetry follows the order of hexagonal, orthorhombic, tetragonal, and cubic phases [24]. We first comparatively investigated the phase information of the parent $\text{SrCoO}_{3-\delta}$ and the doped $\text{SrCo}_{0.95}\text{M}_{0.05}\text{O}_{3-\delta}$ ($\text{M} = \text{Fe}, \text{Sc}, \text{Zn}, \text{Gd}$), which were denoted as SrCo , SrCoFe , SrCoSc , SrCoZn , and SrCoGd , respectively. The XRD patterns in Fig. 1(a)-(c) and Fig. S1 suggest that the proposed doping strategy with various dopants gave rise to three different crystal structures, i.e. 2 H-hexagonal (SrCo , SrCoZn , SrCoGd), tetragonal (SrCoSc) and orthorhombic structures (SrCoFe). In particular, SrCoFe perovskite oxide exhibited an oxygen vacancy (OV)-ordered brownmillerite structure as reflected by the characteristic peak of (002), (141) and (051) in the enlarged XRD pattern (Fig. 1(c) inset) [23]. All the diffraction peaks of the synthesized perovskites can be indexed to the corresponding standard diffraction spectra (JCPDS No. 40-1018, 47-0226 and 34-1475) without observable impurity, indicating single-phase structure. The phase structures were also confirmed by Rietveld refinement analysis. The refined profiles and detailed structural parameters are presented in Fig. S2 and Table S1. The space groups of tetragonal SrCoSc and orthorhombic brownmillerite SrCoFe are $P4/mmm$ and $Ima2$, respectively, whereas the hexagonal SrCo , SrCoGd and SrCoZn belong to $R-3$ group. The schematic illustrations of the three structures are shown in the insets of Fig. 1(a)-(c), in which the frameworks of the hexagonal and tetragonal structures are constructed by the respective face- and corner-shared CoO_6 octahedrons. By contrast, the unique OV-ordered orthorhombic structure is composed of CoO_6 octahedral and Co_2O_4

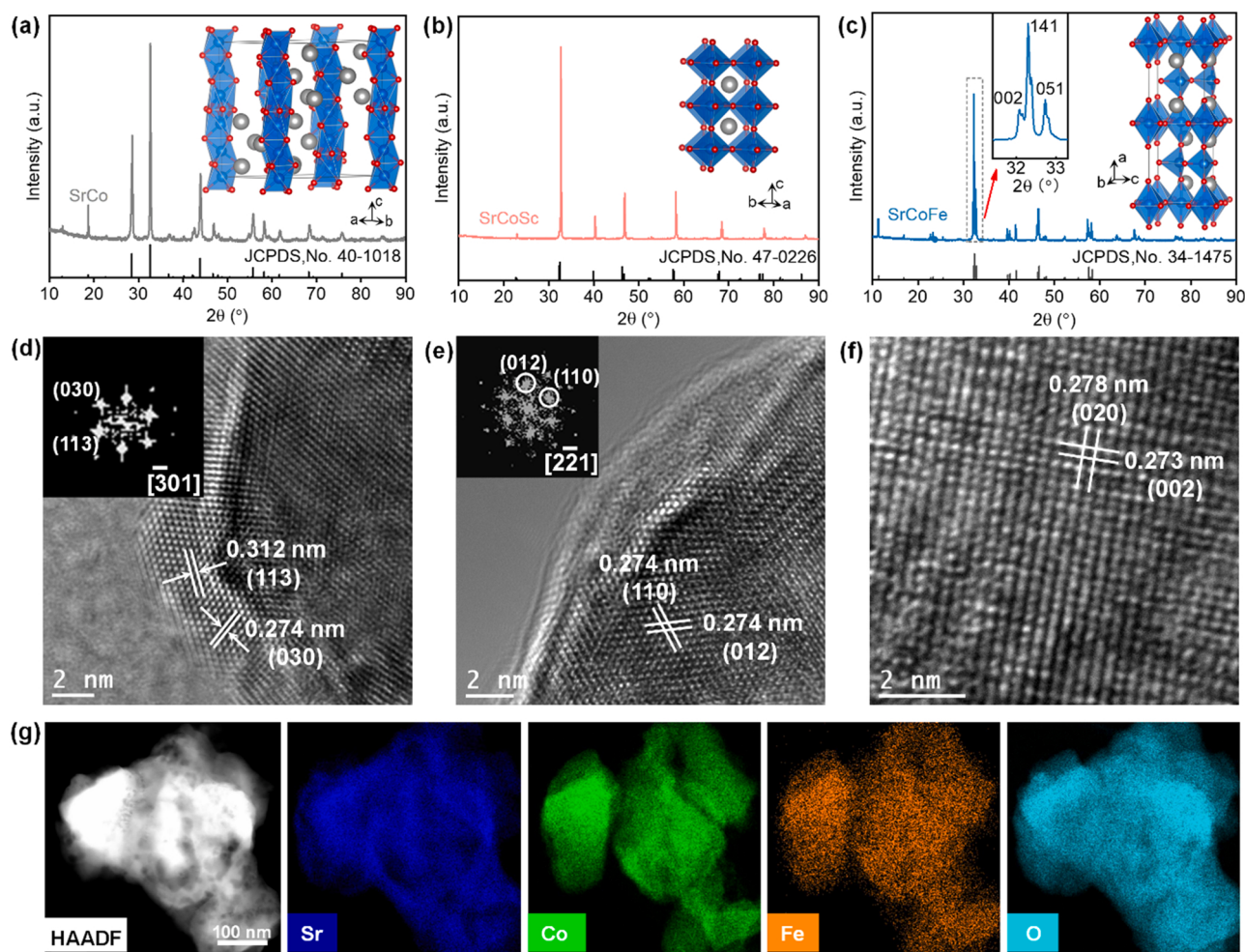


Fig. 1. (a-c) XRD patterns of (a) SrCo , (b) SrCoSc , and (c) SrCoFe ; (d-f) HR-TEM images of (d) SrCo , (e) SrCoSc , and (f) SrCoFe ; (g) HAADF-STEM image of SrCoFe and the corresponding elemental mapping.

tetrahedral layers arranged alternatively along *a* axis, in which the OV is accommodated in the Co_2O_4 tetrahedral layer due to the unsaturated Co₂ coordination. Noteworthy that the Co1 and Co2 represent two different crystallographic positions in the crystal cell. This ordered stacking sequence of the Co_1O_6 and oxygen-depleted Co_2O_4 slabs in brownmillerite structure results in a nominal composition of $\text{Sr}_2\text{Co}_2\text{O}_5$.

To further confirm the structures, we performed the HR-TEM observation. As shown in Fig. 1(d), the fast Fourier transform (FFT) image reflects the hexagonally arranged diffraction spots of the [−301] zone axes. In addition, the observed interplanar spaces of SrCo were 0.312 and 0.274 nm, corresponding to the (113) and (030) facets, respectively. Fig. 1(e) shows a group of lattice spaces (0.274 nm), agreeing well with the (110) and (012) planes of tetragonal SrCoSc. In Fig. 1(f), a group of perpendicular planes with the lattice space of 0.273 and 0.278 nm correspond to the (002) and (020) planes of brownmillerite SrCoFe. Additionally, the overall morphology was examined by high-angle annular dark-field scanning TEM (HAADF-STEM, Fig. 1(g) and Fig. S3) and the catalysts exhibited a similar particle size in the submicron-range with an irregular shape, indicating the negligible influence on morphology and particle size by different dopants. The EDS mapping images show a homogeneous distribution of compositional elements of Sr, Co, M and O, corroborating phase purity and the success of the doping strategy to achieve different structures. The atomic ratio of SrCoM has also been investigated based on the EDS analysis, as shown in Fig. S4. Particularly, the ratios of Co to M dopants are around 19 for all the doped materials, suggesting the homogeneous distribution of the compositional elements and the success of the doping.

Further analyses indicate that the dopant-induced crystal structure alternation resulted in significant changes of lattice parameters (Table S1). Notably, a stretching of Co-O bond in the lattice associated with the phase transition occurred, as evidenced by the remarkable

increments of the average length of Co-O bond from pristine 1.90 Å (hexagonal phase) to 1.94 Å (tetragonal) and 1.97 Å (orthorhombic brownmillerite) phases. This suggests that the structural transition has a significant influence on the coordination environment and electronic structure of B-site Co. Typically, the Co-O bond length is highly relevant to the Co-O covalency which originates from the coupling and hybridization between O 2p and Co 3d orbitals [29]. The incorporation of the dopants and the associated structure change would induce the state of spin coupling between Co 3d and O 2p electrons to change from a lower state to high or intermediate-spin state, as roughly reflected by the slightly increased e_g orbital occupancy of surface Co (Table S2) [30]. The spin state transformation with the Co ionic radius change would inevitably give rise to the Jahn-Teller effect, causing the Co-O bond length elongation and the reduction of Co-O covalent feature [31]. As a result, the longer Co-O bond and high-energy electron accumulation in the antibonding orbitals cause instability in the resultant Co-O system [32]. Thus, less energy is required for lattice O migration and catalytic $\text{Co}^{2+}/\text{Co}^{3+}$ redox cycling. In brief, SrCo-based perovskites with three different crystal structures and specific properties are successfully achieved by a facile substitution strategy, which offers a good platform for the mechanistic study of the intrinsic PMS activation behavior over the perovskite oxide catalysts.

3.2. Catalytic activities

To have a comprehensive evaluation of PMS activation activities in organic degradation performance, we selected 4-hydroxybenzoic acid (HBA), a persistent organic pollutant with acute aquatic toxicity, as a probe contaminant. The degradation reaction was conducted at 25 °C under natural pH environment. As shown in Fig. 2(a), HBA oxidation rates varied with the crystal structure alternation. It was intriguingly found that the brownmillerite SrCoFe delivered the highest capacity for

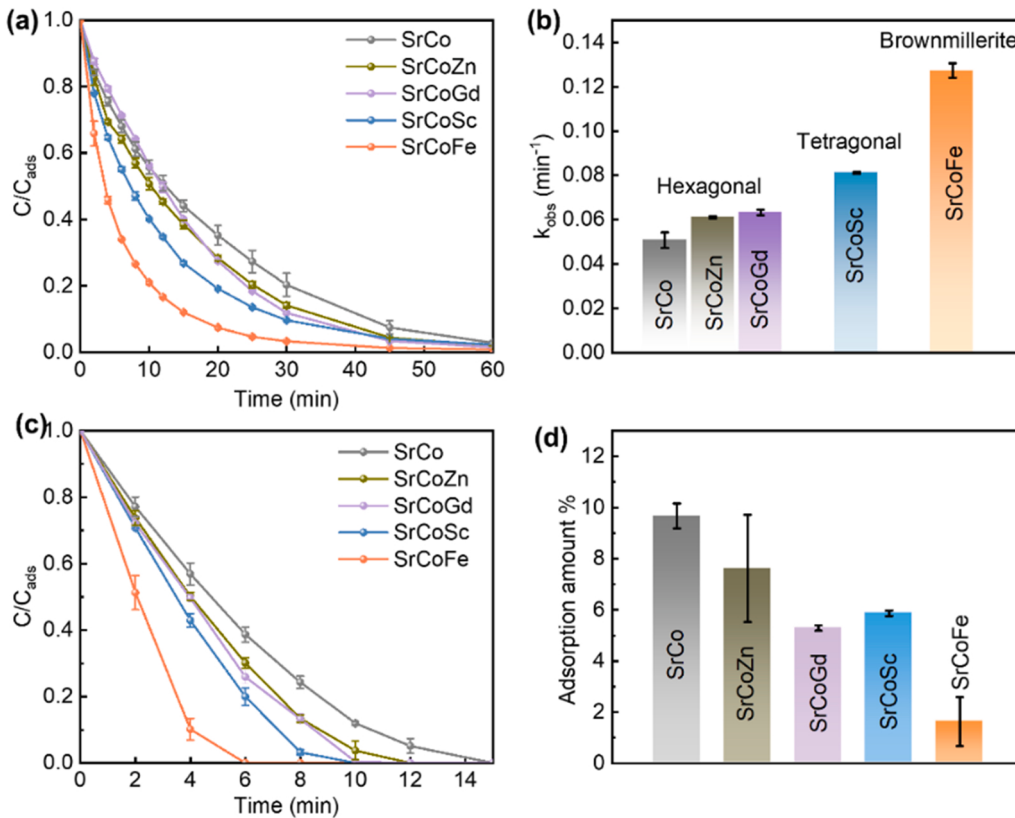


Fig. 2. (a) HBA degradation profiles over SrCoM catalysts and (b) the corresponding pseudo-first order kinetic rate constants; (c) Phenol degradation profiles over SrCoM catalysts; (d) The adsorption amount of HBA by SrCoM catalysts. (Reaction conditions: [HBA] = 50 ppm, [PMS] = 0.5 g L⁻¹, [SrCoM] = 0.1 g L⁻¹, [Phenol] = 20 ppm, T = 25 °C).

PMS activation and HBA oxidation, in which 93% removal of HBA was achieved in 20 min; followed by the tetragonal SrCoSc, exhibiting a moderate performance of 81% HBA degradation. In contrast, other three samples with a hexagonal phase exhibited similar activities, which were all inferior to that of the tetragonal and brownmillerite structures. Specifically, kinetics calculations in Fig. 2(b) indicate that the superior pseudo-first order kinetic constants (k_{obs}) of SrCoFe (0.127 min^{-1}) and SrCoSc (0.081 min^{-1}) were demonstrated, which are almost 2.1 and 1.35 times, respectively, as high as that of the pristine hexagonal perovskite catalysts ($\sim 0.060 \text{ min}^{-1}$). This proves that the crystal phase exerts a significant influence on the PMS activation for HBA oxidation.

To verify if the activity difference among the three structures is relevant to the organics, we employed phenol as another target pollutant to be degraded in the reaction system. As shown in Fig. 2(c), the same order of the phenol degradation efficiency was also observed, suggesting that such an activity distinction stems from the catalyst inherent properties, which will be discussed shortly. In addition, adsorption tests in the absence of PMS were performed to evaluate the contribution of the adsorption to the HBA removal. As shown in Fig. 2(d), trivial amount of HBA (less than 10%) was removed due to the adsorption, which is related to the low specific surface area (SSA) of the catalysts. High temperature sintering endowed SrCoM perovskite oxides with an extreme low SSA (Fig. S5), where the samples with hexagonal structure (SrCo, SrCoZn and SrCoGd) showed similar and slightly higher BET surface areas ($\sim 1 \text{ m}^2 \text{ g}^{-1}$) compared to tetragonal SrCoSc ($0.57 \text{ m}^2 \text{ g}^{-1}$) and brownmillerite SrCoFe ($0.44 \text{ m}^2 \text{ g}^{-1}$). This implies that the dopant-induced crystal structure alternation would affect the texture of the samples [33]. Notably, though the raw hexagonal samples have higher amount of adsorption and more exposed active sites because of the relative larger SSA values, the catalytic removal rates of organics were still sluggish. This firmly proves that the different catalytic performance originates from the crystal structure transition.

The catalytic stabilities of the representative samples of SrCo, SrCoSc, and SrCoFe were evaluated for HBA oxidation (Fig. S6). The pristine SrCo experienced a significant reduction in activity as only 60% of HBA can be removed in the third round reaction. In a strong contrast, SrCoFe and SrCoSc presented better catalytic stabilities with only a

slight decrease in activity. Particularly, the degradation efficiencies for SrCoFe were 96%, 95% and 91% in the first, second, and third rounds, respectively. This suggests that the doping and the associated phase transition are beneficial for the stability of SrCoM.

3.3. Identification of reaction pathways and potential reactive oxygen species

To reveal the reaction mechanism and determine the involved ROS, we introduced chemical probes including methanol, *tert*-butanol (tBA), *p*-benzoquinone (*p*BQ), sodium azide (NaN_3) into the reaction system as the scavengers of sulfate radical ($\text{SO}_4^{\cdot-}$), hydroxyl radical ($\cdot\text{OH}$), super oxide radical ($\text{O}_2^{\cdot-}$), and singlet oxygen (${}^1\text{O}_2$), respectively. Taking SrCoFe as an example, the addition of 200 mM tBA or 3 mM *p*BQ led to a slight inhibition of HBA degradation (Fig. 3(a)), while the HBA removal was largely retarded with a only $\sim 40\%$ removal in 60 min in the presence of 200 mM methanol, suggesting the primary contribution of highly oxidative $\text{SO}_4^{\cdot-}$ instead of other radicals ($\cdot\text{OH}$ and $\text{O}_2^{\cdot-}$). When 3 mM NaN_3 was added, the HBA degradation was almost suspended with only 15% removal in 60 min. At first glance, singlet oxygen might play a vital role in HBA oxidation due to the notable suppression effect. But the nature of non-selectivity of NaN_3 for radical quenching ($k = 1.2 \times 10^{10} \text{ M}^{-1} \text{ s}^{-1}$ for $\text{SO}_4^{\cdot-}$; $k = 2.52 \times 10^9 \text{ M}^{-1} \text{ s}^{-1}$ for $\cdot\text{OH}$) and singlet oxygen scavenging ($k = 1.0 \times 10^9 \text{ M}^{-1} \text{ s}^{-1}$ for ${}^1\text{O}_2$) may mislead the quenching results [34]. In addition, NaN_3 can trap electrons thus hamper the electron transfer process. It was also reported that NaN_3 is also highly active to react with and decompose PMS [35,36]. Given this, the dominant role of $\text{SO}_4^{\cdot-}$ in the system can be determined but it is difficult to know if the non-radical processes (singlet oxygen process and direct electron transfer mechanism) participate in the PMS activation and organic oxidation processes. The ROS identification and potential reaction pathway require further verification.

In-situ EPR spectra were collected using DMPO and TEMP as spin-trapping reagents for $\cdot\text{OH}$, $\text{SO}_4^{\cdot-}$ and ${}^1\text{O}_2$ to confirm the involved ROS. As shown in Fig. 3(b), the triplet signals can be attributed to the formation of 2,2,6,6-tetramethyl-4-piperidinol-N-oxyl (TEMP-OX) oxidized by ${}^1\text{O}_2$. Comparing to the blank test (PMS only), the peak intensity tends

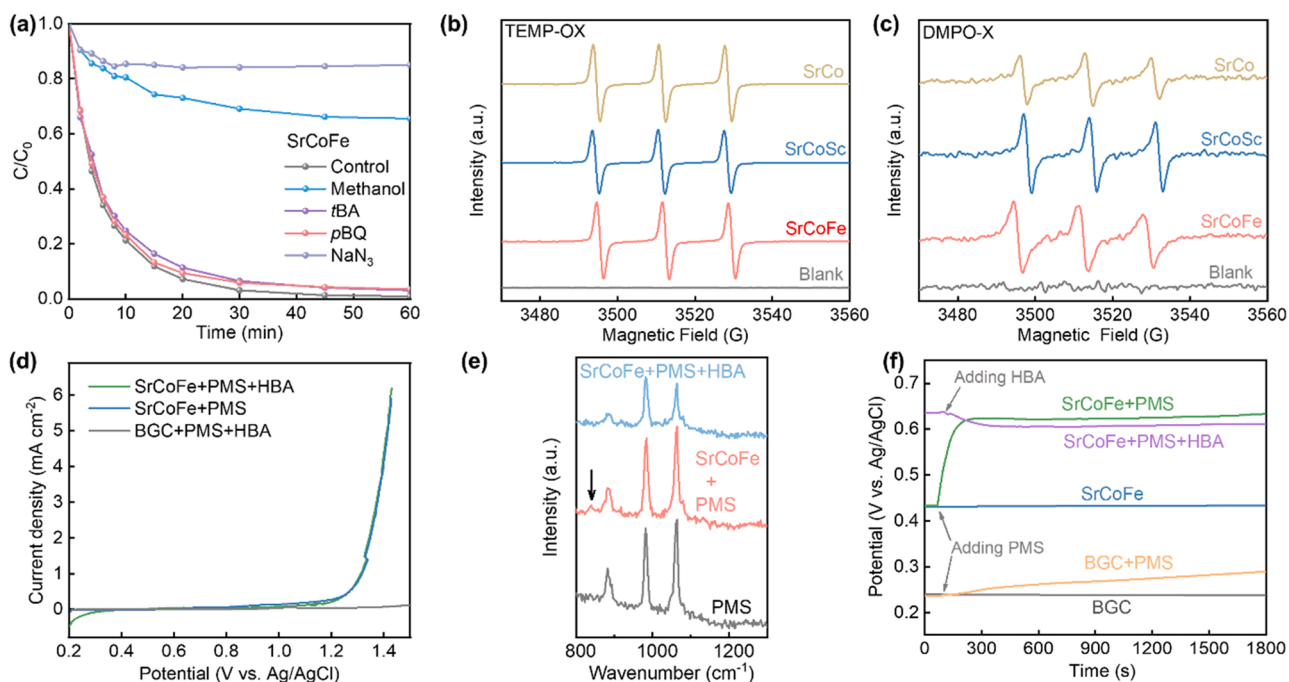


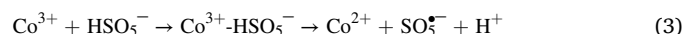
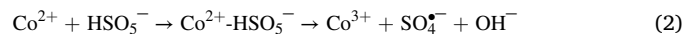
Fig. 3. (a) Quenching experiments for HBA oxidation over SrCoFe; (b-c) EPR spectra using (b) TEMP and (c) DMPO as trapping agents; (d) LSC curves over BGC and SrCoFe electrodes with PMS and/or HBA; (e) In-situ Raman spectra under different conditions; (f) Open-circuit potential curves on BGC and SrCoFe electrodes under different conditions.

to increase intensively with the simultaneous presence of SrCoM, PMS and HBA. This demonstrates the generation of ${}^1\text{O}_2$ via PMS activation over the SrCoM catalyst [15]. The spectra using DMPO were shown in Fig. 3(c). No signals of DMPO- SO_4^{2-} and DMPO- $\cdot\text{OH}$ were observed in the system, but DMPO was directly oxidized into 5,5-dimethyl-2-pyrrolidone-N-oxyl (DMPO-X) in the co-presence of SrCoM and PMS,³⁸ indicating the strong oxidation capacity of the reaction system. Previous studies suggested that not only radicals could lead to the formation of DMPO-X, DMPO can also be oxidized directly in the system via the direct electron transfer among organics, catalyst, and PMS to form DMPO-X [36,37]. Therefore, PMS activation via a direct electron transfer process should be evaluated as well.

In regard to the direct electron transfer mechanism, PMS prefers binding with the catalyst and then attacks organic molecules by depriving electrons without generation ROS [38]. Electrochemical approaches, such as LSV and EIS, are the frequently used techniques to characterize the electron transfer process [39]. Herein, LSV was used to monitor the electron transfer process under different conditions. As shown in Fig. 3(d), the current response of bare glassy carbon (BGC) electrode in PMS (0.5 g L⁻¹) and HBA (50 ppm) solution was negligible. By contrast, the coated electrode with SrCoFe in PMS electrolyte exhibited a remarkable current increment, demonstrating strong electron transfer activity and interaction between SrCoFe and PMS. However, the addition of HBA into the system did not induce any perceptible changes, implying that the direct electron transfer degradation mechanism (electron donation process from organics) was barely involved in the reaction. Based on the above analysis, it can be concluded that, in this radical oxidation process, sulfate radicals other than singlet oxygen are making the major contribution to the highly oxidative capability of the SrCoM/PMS system.

Despite that the direct electron transfer mechanism was not involved, a strong interaction and electron migration between PMS and SrCoFe catalyst were observed in the PMS activation process as aforementioned. Such an intimate interaction was further explored using *in situ* Raman and chronopotentiometry measurements to explain the detailed PMS activation behavior over SrCoM. As shown in the Raman spectra (Fig. 3(e)), the peaks centered at 882 and 1065 cm⁻¹ can be ascribed to HSO_5^- , while the one at 983 cm⁻¹ is related to SO_4^{2-} , and no other peaks were found in the sole PMS solution [40]. However, with the introduction of SrCoFe catalyst into the PMS solution, a newly formed peak located at 837 cm⁻¹ appeared (marked by the arrow). The new peak can be attributed to the peroxy species (TM-HSO₅) bonded to the B-site Co on the perovskite surface [40]. The PMS experienced a rapid consumption with the presence of HBA as reflected by the sharp reduction of the peak intensity at 1065 cm⁻¹. Besides, the peak of peroxy species was also weakened when HBA was added into the system. This indicates that PMS molecules were first catalytically formed as a surface complex (TM-HSO₅) and then underwent a series of subsequent processes to evolve into ROS. Fig. 3(f) shows the catalyst potential based on the chronopotentiometry technique under different conditions. The potential of BGC remained the lowest (238 mV vs. Ag/AgCl) and increased sluggishly since introducing PMS in electrolyte. In contrast, the coated electrode with SrCoFe exhibited a much higher potential (430 mV vs. Ag/AgCl) and a prompt improvement in the presence of PMS, which was finally stabilized at around 630 mV. However, the potential of the catalyst showed an insignificant change with the addition of HBA in the system, further confirming the absence of the direct electron transfer pathway from HBA. Based on the above results, it can be concluded that PMS initially coordinated with Co on the catalyst surface to form a surface complex with higher potential, which might be more active and conducive for activation. Then the surface ligands underwent an electron transfer process from Co^{2+} to the ligand for ROS (SO_4^{2-} and ${}^1\text{O}_2$) formation and fulfilled the $\text{Co}^{2+}/\text{Co}^{3+}$ redox cycle (Eqs. 2–4). For the other SrCoM samples with tetragonal and hexagonal phases, quenching experiments (Fig. S7) showed the similar inhibition effect of each chemical scavenger, suggesting structure alternation has no influence on

PMS activation mechanism though with a distinct activity variation.



3.4. The origin of the catalytic activity

To figure out the decisive factor that differentiates the PMS activation activities of SrCoM, we tried to correlate a series of inherent properties from catalysts, such as PMS adsorption, catalyst defects, conductivity, electronic structure, and redox property, with the catalytic performance. Given the required intimate interaction between PMS and the catalyst during the activation, the adsorption of PMS on a catalyst is of vital importance and thus evaluated. It was reported that the hydroxyl groups (-OH) on perovskite oxide surface could act as the active sites to facilitate PMS adsorption via hydrogen bonding [9]. Therefore, XPS was conducted to reveal the relative content of surface -OH. Based on the O 1 s deconvolution spectra in Fig. 4(a) and Fig. S8(a), the peaks located at ~528.5, 530.0, 531.0 and 532.2 eV are corresponding to the lattice oxygen (O^{2-}), OV-related surface oxygen species ($\text{O}^-/\text{O}_2^{2-}$), surface -OH and adsorbed molecular water/carbonates, respectively [41]. As shown in Fig. 4(b), SrCoZn with an obviously higher content of surface -OH than the other samples presented inferior performance for PMS activation. This demonstrates that the surface -OH was not the decisive factor contributing to PMS activation. More importantly, surface transition metal sites are known as more typical adsorption sites in oxide-based catalysts. According to Sabatier's principle, the adsorption between surface Co and PMS is through σ -bonding and the favorable bonding strength should be neither too strong nor too weak to promote PMS activation and ROS generation, which can be realized at the e_g orbital electron filling number of Co close to unity [8,9]. In light of this, the e_g filling number of surface Co was calculated and given in Table S2. All the samples with different structures presented e_g values of around 1.2 that is close to unity, indicating a good adsorption capacity. More importantly, the similar value of e_g suggests that the adsorption capacity for SrCoM catalysts remain close and was not the control step for PMS activation. This is also confirmed by FT-IR investigation in terms of the PMS adsorption capacity over each sample (Fig. 4(c)). The IR band at about 1096 cm⁻¹ can be ascribed to the S-O bond stretching in PMS molecules, and a slight red shift was observed for all PMS/SrCoM systems owing to the adsorption of PMS on catalyst surface [36]. Noteworthy that all the catalysts exhibited a negligible difference in PMS adsorption due to a similar degree of the red-shift in FT-IR spectra, suggesting the similar adsorption abilities of SrCoM.

Besides, the crucial role of OV in AOPs has been intensively studied [42–45]. Wang et al. demonstrated that OV as a Lewis acid site showed strong tendency to adsorb single-bond oxygen of an ozone molecule and cause its direct disassociation to produce ROS [44]. Analogously, PMS activation also relies on the cleavage of O-O bond to yield ROS [3]. Miao et al. [15] and Li et al. [46] manifested that OV was responsible for the ${}^1\text{O}_2$ generation during PMS activation. Herein, we evaluated the surface oxygen defect of SrCoM. As depicted in Fig. 4(b), the OV-related $\text{O}^-/\text{O}_2^{2-}$ varied significantly with the phase change. Tetragonal SrCoSc showed the highest OV content of 32.26%, which was almost two times higher than hexagonal SrCo (16.44%) and brownmillerite SrCoFe (14.82%). The remarkable improvement of oxygen defects for tetragonal SrCoSc may provide additional active sites for PMS activation. However, there is no direct correlation between the PMS activation activity and surface OV content, implying its non-dominant role.

Moreover, PMS activation greatly relies on the charge migration and redox cycling as above mentioned, charge transfer resistance (R_{ct}) should be another important factor that may affect the catalytic

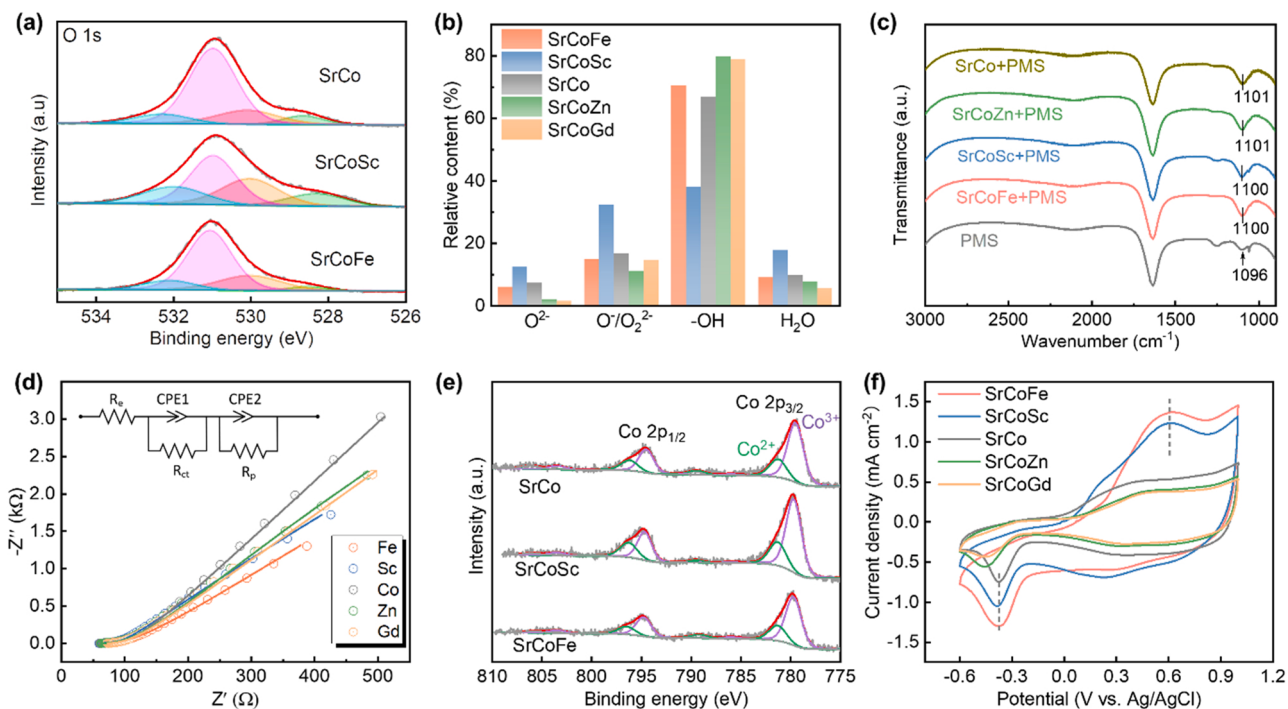
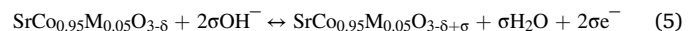


Fig. 4. (a) XPS spectra of O1s and the deconvolution profiles; (b) the relative content of surface oxygen species obtained from XPS analysis; (c) FTIR spectra demonstrating the PMS complexation on the catalyst surface; (d) EIS spectra of SrCoM in 0.1 M Na₂SO₄ electrolyte; (e) XPS spectra of Co 2p and the deconvolution profiles; (f) CV curves of SrCoM showing the Co²⁺/Co³⁺ redox capabilities.

performance. EIS (Fig. 4(d)) was obtained to evaluate the effect of R_{ct} on PMS activation performance. By constructing an equivalent circuit including the components of solution resistance (R_s), charger-transfer resistance (R_{ct}) and two constant-phase elements (CPE), the R_{ct} values of SrCoFe, SrCoSc, SrCo, SrCoZn and SrCoGd were 81.05, 45.66, 86.47, 66.73 and 75.88 Ω, respectively. It is interesting to find that the tetragonal SrCoSc exhibits the best charge-transfer ability instead of the brownmillerite with the highest catalytic activity, indicating that the charge transfer is not the main factor to control the PMS activation. In general, the electronic conductivity of ABO₃ perovskite oxides depends on strong overlapping between the d orbital of B-site cations and O 2p orbital [47]. It is proved that the higher symmetric crystal structure would induce more dispersive conduction band (Co 3d band) that overlapped well with O 2p band, which is conducive for the electron transfer [20]. This explains our finding that the tetragonal SrCoSc with higher symmetric structure showed the relative lower charge transfer resistance than the orthorhombic and hexagonal structures. Such a superior electronic transfer capacity could be one of the factors benefiting the PMS activation.

The oxidation states and redox property of transition metals in perovskite are essential to catalysis as they directly facilitate the chemical reaction [9,48–50]. As for PMS activation by a perovskite oxide, it is known that Co²⁺/Co³⁺ as the most efficient redox pair demonstrated the exceptional activity for PMS activation [50]. The oxidation states of Co are explored based on Co 2p spectra (Fig. 4(e) and Fig. S8(b)). Both Co²⁺ (at the binding energies of 781.4 and 796.3 eV) and Co³⁺ (at the binding energies of 779.7 and 794.7 eV) were detected. The ratio of Co²⁺/Co³⁺ and the average valence were summarized in Table S2. The tetragonal SrCoSc and brownmillerite SrCoFe showed a relative higher content of Co²⁺ than the hexagonal SrCo, suggesting that SrCoSc and SrCoFe have greater propensity to secure Co at lower valence states, which is the desirable property for PMS activation. The CV curves (Fig. 4(f)) were recorded in 0.5 M Na₂SO₄ solution to characterize the redox property of Co²⁺/Co³⁺, and brownmillerite SrCoFe and tetragonal SrCoSc exhibited a pair of distinct redox peaks at around -0.38 and 0.61 V vs. Ag/AgCl, corresponding to the respective

reduction and oxidation processes between Co³⁺ and Co²⁺. On the contrary, the almost flat anodic peak and the significantly reduced cathodic peak of the hexagonal structures were observed. The redox peak current densities of SrCoM reflect that the Co²⁺/Co³⁺ redox capacity follows the order of brownmillerite > tetragonal > hexagonal structures, agreeing well with their catalytic performance. Of significance, the Co²⁺ oxidation and Co³⁺ reduction are generally accompanied by the oxygen ion insertion and extraction from the lattice to maintain the charge neutrality of SrCoM catalysts, which can be illustrated by Eq. (5) [51].



In other words, the redox ability of SrCoM is tightly related to the lattice oxygen migration activity and, accordingly, the highest current densities of SrCoFe in both the oxidation and reduction regimes are indicative of the fastest oxygen intercalation and extraction. In this manner, the hexagonal samples owned the worst lattice migration ability while the tetragonal SrCoSc presented a moderate ability.

To further corroborate this, the lattice oxygen diffusion coefficients (D_o) of the representative samples were measured through chronoamperometry, and the results are shown in Fig. 5(a). By employing a bounded three-dimensional model previously reported [51,52], the D_o values were determined to be 2.1×10^{-10} , 3.7×10^{-10} , and 6.1×10^{-10} cm² s⁻¹ for SrCo, SrCoSc and SrCoFe, respectively, consistent with the previous literature results for strontium cobaltites [52]. The oxygen diffusion coefficients of SrCoFe and SrCoSc are 2.9 and 1.8 times faster than SrCo, respectively, which correlates well with their improvements in the HBA oxidation kinetics (Fig. 5(b)). Particularly, the remarkably accelerated lattice oxygen ion diffusion of brownmillerite and tetragonal structures can be attributed to the reduced covalency of Co-O bond induced by the structural transition as discussed above. Owing to the elongated Co-O bond and the accumulation of high-energy electrons in the antibonding orbitals, the less covalent Co-O becomes weaker, which favors the oxygen anion diffusion. As a result, the intrinsic redox cycling of Co²⁺/Co³⁺ can be more feasible benefiting from the enhanced

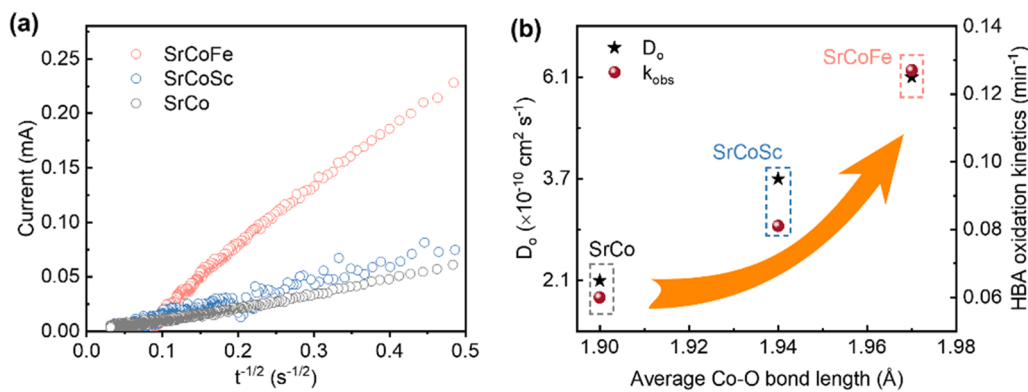


Fig. 5. (a) The chronoamperometry data (i vs $t^{1/2}$) used for the calculation of oxygen ion diffusion coefficients; (b) The correlations of oxygen ion diffusion coefficient and HBA oxidation kinetics with the average Co-O bond length.

processes of oxygen ion insertion and extraction from the perovskite lattice. Such a favorable redox ability of SrCoFe can facilitate more efficient PMS activation. To be more specific, the activation process starts from the adsorption of PMS molecules on the catalyst surface (Co^{2+} active sites) to form surface ligands ($\text{Co}^{2+}\text{-HSO}_5^-$). The surface ligands subsequently experience a decomposition process by depriving electrons from Co^{2+} to produce highly oxidative radicals for water remediation, while the Co^{2+} active sites have been oxidized to Co^{3+} . Then the regeneration of Co^{2+} active sites from Co^{3+} (Eq. 3) is often sluggish, thus limiting the overall PMS activation efficiency. However, with the assistance of the elongated Co-O bond system and its associated accelerated lattice oxygen diffusivity, the regeneration of surface Co^{2+} active sites and the redox cycling of $\text{Co}^{2+}/\text{Co}^{3+}$ can be more feasible. Consequently, the PMS activation performance has been improved. Given this, despite the impact factors of perovskite for PMS activation remain complex, the Co-O bond length in SrCoM perovskite oxides could be identified as a good activity descriptor for PMS activation.

4. Conclusions

In summary, $\text{SrCo}_{0.95}\text{M}_{0.05}\text{O}_{3-\delta}$ perovskite oxides with three different crystal structures (hexagonal, tetragonal and orthorhombic brownmillerite phases) were successfully prepared via a substitution strategy to replace 5% cobalt by foreign elements. The phase structural alternation induces a significant variation in physicochemical properties and catalytic performance, and the orthorhombic brownmillerite structure exhibited the best PMS activation activity followed by tetragonal and hexagonal structures. A straightforward correlation between the PMS activation activity, $\text{Co}^{2+}/\text{Co}^{3+}$ redox ability and bond length of Co-O was established. The structural transition from hexagonal to brownmillerite leads to the gradual increment of the average Co-O bond length because of the reduced covalent feature. As a result, the Co-O bond length is identified as the most important activity indicator for PMS activation. The elongated Co-O bond in $\text{SrCo}_{0.95}\text{M}_{0.05}\text{O}_{3-\delta}$ system favors the lattice oxygen diffusion and the associated redox ability. This important observation can provide guideline to design other new perovskite oxide catalysts by using their feasible lattice oxygen diffusivity and redox capacity to promote their catalytic effects for more advanced applications.

CRediT authorship contribution statement

Kai Wang: Investigation, Methodology, Data curation, Writing – original draft. **Chen Han:** Conceptualization, Methodology. **Fuping Li:** Investigation, Methodology. **Yu Liu:** Data curation. **Zongping Shao:** Supervision, Writing – review & editing. **Lihong Liu:** Investigation, Methodology. **Shaobin Wang & Shaomin Liu:** Supervision, Writing – review & editing, Funding acquisition.

Declaration of Competing Interest

The authors declare that they have no known competing financial interests or personal relationships that could have appeared to influence the work reported in this paper.

Data Availability

Data will be made available on request.

Acknowledgements

The authors would like to acknowledge the funding from the Fundamental Research Fund for the Central University of China (Buctrc202115) and Australia Research Council Discovery Project (DP180103861).

Appendix A. Supporting information

Supplementary data associated with this article can be found in the online version at doi:10.1016/j.apcatb.2022.121990.

References

- [1] L. Liu, Q. Liu, Y. Wang, J. Huang, W. Wang, L. Duan, X. Yang, X. Yu, X. Han, N. Liu, Nonradical activation of peroxydisulfate promoted by oxygen vacancy-laden NiO for catalytic phenol oxidative polymerization, *Appl. Catal. B Environ.* 254 (2019) 166–173.
- [2] S. Liu, Z. Zhang, F. Huang, Y. Liu, L. Feng, J. Jiang, L. Zhang, F. Qi, C. Liu, Carbonized polyaniline activated peroxymonosulfate (PMS) for phenol degradation: Role of PMS adsorption and singlet oxygen generation, *Appl. Catal. B Environ.* 286 (2021), 119921.
- [3] P. Cai, J. Zhao, X. Zhang, T. Zhang, G. Yin, S. Chen, C.-L. Dong, Y.-C. Huang, Y. Sun, D. Yang, B. Xing, Synergy between cobalt and nickel on NiCo_2O_4 nanosheets promotes peroxymonosulfate activation for efficient norfloxacin degradation, *Appl. Catal. B Environ.* 306 (2022), 121091.
- [4] M. You, L. Gui, X. Ma, Z. Wang, Y. Xu, J. Zhang, J. Sun, B. He, L. Zhao, Electronic tuning of SrIrO_3 perovskite nanosheets by sulfur incorporation to induce highly efficient and long-lasting oxygen evolution in acidic media, *Appl. Catal. B Environ.* 298 (2021), 120562.
- [5] K. Wei, A. Armutlulu, Y. Wang, G. Yao, R. Xie, B. Lai, Visible-light-driven removal of atrazine by durable hollow core-shell $\text{TiO}_2@\text{LaFeO}_3$ heterojunction coupling with peroxymonosulfate via enhanced electron-transfer, *Appl. Catal. B Environ.* 303 (2022), 120889.
- [6] M. Zhu, D. Guan, Z. Hu, H.-J. Lin, C.-T. Chen, H.-S. Sheu, S. Wang, J. Zhou, W. Zhou, Z. Shao, Synergistic effects in ordered Co oxides for boosting catalytic activity in advanced oxidation processes, *Appl. Catal. B Environ.* 297 (2021), 120463.
- [7] S.B. Hammouda, F. Zhao, Z. Safaei, V. Srivastava, D. Lakshmi Ramasamy, S. Iftekhar, S. Kallio, M. Sillanpää, Degradation and mineralization of phenol in aqueous medium by heterogeneous monopersulfate activation on nanostructured cobalt based-perovskite catalysts ACoO_3 ($\text{A}=\text{La}, \text{Ba}, \text{Sr}$ and Ce): Characterization, kinetics and mechanism study, *Appl. Catal. B Environ.* 215 (2017) 60–73.
- [8] J. Suntivich, K.J. May, H.A. Gasteiger, J.B. Goodenough, Y. Shao-Horn, A perovskite oxide optimized for oxygen evolution catalysis from molecular orbital principles, *Science* 334 (2011) 1383.

- [9] C. Su, X. Duan, J. Miao, Y. Zhong, W. Zhou, S. Wang, Z. Shao, Mixed conducting perovskite materials as superior catalysts for fast aqueous-phase advanced oxidation: a mechanistic study, *ACS Catal.* 7 (2017) 388–397.
- [10] J. Miao, J. Sunarso, X. Duan, W. Zhou, S. Wang, Z. Shao, Nanostructured Co-Mn containing perovskites for degradation of pollutants: Insight into the activity and stability, *J. Hazard. Mater.* 349 (2018) 177–185.
- [11] Y. Rao, Y. Zhang, F. Han, H. Guo, Y. Huang, R. Li, F. Qi, J. Ma, Heterogeneous activation of peroxymonosulfate by LaFeO_3 for diclofenac degradation: DFT-assisted mechanistic study and degradation pathways, *Chem. Eng. J.* 352 (2018) 601–611.
- [12] Q. Ji, L. Bi, J. Zhang, H. Cao, X.S. Zhao, The role of oxygen vacancies of ABO_3 perovskite oxides in the oxygen reduction reaction, *Energy Environ. Sci.* 13 (2020) 1408–1428.
- [13] P. Gao, X. Tian, Y. Nie, C. Yang, Z. Zhou, Y. Wang, Promoted peroxymonosulfate activation into singlet oxygen over perovskite for ofloxacin degradation by controlling the oxygen defect concentration, *Chem. Eng. J.* 359 (2019) 828–839.
- [14] J. Miao, J. Li, J. Dai, D. Guan, C. Zhou, W. Zhou, X. Duan, S. Wang, Z. Shao, Postsynthesis oxygen nonstoichiometric regulation: a new strategy for performance enhancement of perovskites in advanced oxidation, *Ind. Eng. Chem. Res.* 59 (2019) 99–109.
- [15] J. Miao, X. Duan, J. Li, J. Dai, B. Liu, S. Wang, W. Zhou, Z. Shao, Boosting performance of lanthanide magnetism perovskite for advanced oxidation through lattice doping with catalytically inert element, *Chem. Eng. J.* 355 (2019) 721–730.
- [16] M. Zhu, J. Miao, X. Duan, D. Guan, Y. Zhong, S. Wang, W. Zhou, Z. Shao, Postsynthesis growth of CoOOH nanostructure on $\text{SrCo}_{0.6}\text{Ti}_{0.4}\text{O}_{3-\delta}$ perovskite surface for enhanced degradation of aqueous organic contaminants, *ACS Sustain. Chem. Eng.* 6 (2018) 15737–15748.
- [17] W. Zhou, J. Sunarso, Enhancing bi-functional electrocatalytic activity of perovskite by temperature shock: a case study of $\text{LaNiO}_{3-\delta}$, *J. Phys. Chem. Lett.* 4 (2013) 2982–2988.
- [18] S. She, J. Yu, W. Tang, Y. Zhu, Y. Chen, J. Sunarso, W. Zhou, Z. Shao, Systematic study of oxygen evolution activity and stability on $\text{La}_{1-x}\text{Sr}_x\text{FeO}_{3-\delta}$ perovskite electrocatalysts in alkaline media, *ACS Appl. Mater. Interfaces* 10 (2018) 11715–11721.
- [19] W. Wang, Y. Yang, D. Huan, L. Wang, N. Shi, Y. Xie, C. Xia, R. Peng, Y. Lu, An excellent OER electrocatalyst of cubic $\text{SrCoO}_{3-\delta}$ prepared by a simple F-doping strategy, *J. Mater. Chem. A* 7 (2019) 12538–12546.
- [20] P. Li, S. Ouyang, G. Xi, T. Kako, J. Ye, The effects of crystal structure and electronic structure on photocatalytic H_2 evolution and CO_2 reduction over two phases of perovskite-structured NaNbO_3 , *J. Phys. Chem. C* 116 (2012) 7621–7628.
- [21] A. Nakatsuka, A. Yoshiasa, N. Nakayama, T. Mizota, H. Takei, Oxygen-deficient strontium cobaltate, $\text{SrCo}_{2.64}$, *Acta Crystallogr. Sect. C* 60 (2004) i59–i60.
- [22] H. Jeen, W.S. Choi, J.W. Freeland, H. Ohta, C.U. Jung, H.N. Lee, Topotactic phase transformation of the brownmillerite $\text{SrCoO}_{2.5}$ to the perovskite $\text{SrCoO}_{3-\delta}$, *Adv. Mater.* 25 (2013) 3651–3656.
- [23] P. Zeng, Z. Shao, S. Liu, Z.P. Xu, Influence of M cations on structural, thermal and electrical properties of new oxygen selective membranes based on $\text{SrCo}_{0.95}\text{Mn}_{0.05}\text{O}_{3-\delta}$ perovskite, *Sep. Purif. Technol.* 67 (2009) 304–311.
- [24] P. Zeng, R. Ran, Z. Chen, W. Zhou, H. Gu, Z. Shao, S. Liu, Efficient stabilization of cubic perovskite $\text{SrCoO}_{3-\delta}$ by site low concentration scandium doping combined with sol-gel synthesis, *J. Alloy. Compd.* 455 (2008) 465–470.
- [25] H.A. Tahini, X. Tan, U. Schwingenschlögl, S.C. Smith, Formation and migration of oxygen vacancies in SrCoO_3 and their effect on oxygen evolution reactions, *ACS Catal.* 6 (2016) 5565–5570.
- [26] J. Rodríguez, J.M. González-Calbet, Rhombohedral $\text{Sr}_2\text{Co}_2\text{O}_5$: a new $\text{A}_2\text{M}_2\text{O}_5$ phase, *Mater. Res. Bull.* 21 (1986) 429–439.
- [27] J. Rodriguez, J.M. Gonzalez-Calbet, J.C. Grenier, J. Pannetier, M. Anne, Phase transitions in $\text{Sr}_2\text{Co}_2\text{O}_5$: a neutron thermodiffraction study, *Solid State Commun.* 62 (1987) 231–234.
- [28] Z.Q. Deng, W.S. Yang, W. Liu, C.S. Chen, Relationship between transport properties and phase transformations in mixed-conducting oxides, *J. Solid State Chem.* 179 (2006) 362–369.
- [29] X.-T. Wang, T. Ouyang, L. Wang, J.-H. Zhong, T. Ma, Z.-Q. Liu, Redox-inert Fe^{3+} ions in octahedral sites of Co-Fe spinel oxides with enhanced oxygen catalytic activity for rechargeable zinc-air batteries, *Angew. Chem. Int. Ed.* 58 (2019) 13291–13296.
- [30] H. Takahashi, F. Munakata, M. Yamanaka, Ab initio study of the electronic structures in LaCoO_3 - SrCoO_3 systems, *Phys. Rev. B* 57 (1998) 15211–15218.
- [31] D. Louca, J.L. Sarrao, Dynamical Disorder of spin-induced Jahn-Teller orbitals with the insulator-metal transition in cobaltites, *Phys. Rev. Lett.* 91 (2003), 155501.
- [32] Y. Tong, J. Wu, P. Chen, H. Liu, W. Chu, C. Wu, Y. Xie, Vibronic superexchange in double perovskite electrocatalyst for efficient electrocatalytic oxygen evolution, *J. Am. Chem. Soc.* 140 (2018) 11165–11169.
- [33] J. Xu, Y. Zhang, X. Xu, X. Fang, R. Xi, Y. Liu, R. Zheng, X. Wang, Constructing $\text{La}_2\text{B}_2\text{O}_7$ ($\text{B} = \text{Ti}, \text{Zr}, \text{Ce}$) compounds with three typical crystalline phases for the oxidative coupling of methane: the effect of phase structures, superoxide anions, and alkalinity on the reactivity, *ACS Catal.* 9 (2019) 4030–4045.
- [34] Y. Yang, G. Banerjee, G.W. Brudvig, J.-H. Kim, J.J. Pignatello, Oxidation of organic compounds in water by unactivated peroxymonosulfate, *Environ. Sci. Technol.* 52 (2018) 5911–5919.
- [35] W. Ren, L. Xiong, X. Yuan, Z. Yu, H. Zhang, X. Duan, S. Wang, Activation of peroxydisulfate on carbon nanotubes: Electron transfer mechanism, *Environ. Sci. Technol.* (2019).
- [36] K.Z. Huang, H.J. Zhang, Direct electron transfer-based peroxymonosulfate activation by iron-doped manganese oxide ($\delta\text{-MnO}_2$) and the development of galvanic oxidation processes (GOPs), *Environ. Sci. Technol.* 53 (2019) 12610–12620.
- [37] J. Huang, Y. Dai, K. Singewald, C.-C. Liu, S. Saxena, H. Zhang, Effects of MnO_2 of different structures on activation of peroxymonosulfate for bisphenol A degradation under acidic conditions, *Chem. Eng. J.* 370 (2019) 906–915.
- [38] C. Han, X. Duan, M. Zhang, W. Fu, X. Duan, W. Ma, S. Liu, S. Wang, X. Zhou, Role of electronic properties in partition of radical and nonradical processes of carbocatalysis toward peroxymonosulfate activation, *Carbon* 153 (2019) 73–80.
- [39] X. Zhou, Z. Zeng, G. Zeng, C. Lai, R. Xiao, S. Liu, D. Huang, L. Qin, X. Liu, B. Li, H. Yi, Y. Fu, L. Li, Z. Wang, Persulfate activation by swine bone char-derived hierarchical porous carbon: Multiple mechanism system for organic pollutant degradation in aqueous media, *Chem. Eng. J.* 383 (2020), 123091.
- [40] T. Zhang, H. Zhu, J.-P. Croué, Production of sulfate radical from peroxymonosulfate induced by a magnetically separable CuFe_2O_4 spinel in water: Efficiency, stability, and mechanism, *Environ. Sci. Technol.* 47 (2013) 2784–2791.
- [41] Y. Zhu, W. Zhou, Y. Zhong, Y. Bu, X. Chen, Q. Zhong, M. Liu, Z. Shao, A perovskite nanorod as bifunctional electrocatalyst for overall water splitting, *Adv. Energy Mater.* 7 (2016), 1602122.
- [42] J. Li, D. Chu, H. Dong, D.R. Baker, R. Jiang, Boosted oxygen evolution reactivity by igniting double exchange interaction in spinel oxides, *J. Am. Chem. Soc.* 142 (2019) 50–54.
- [43] Y. Zhu, W. Zhou, J. Sunarso, Y. Zhong, Z. Shao, Phosphorus-doped perovskite oxide as highly efficient water oxidation electrocatalyst in alkaline solution, *Adv. Funct. Mater.* 26 (2016) 5862–5872.
- [44] Y. Wang, L. Chen, H. Cao, Z. Chi, C. Chen, X. Duan, Y. Xie, F. Qi, W. Song, J. Liu, S. Wang, Role of oxygen vacancies and Mn sites in hierarchical $\text{Mn}_2\text{O}_3/\text{LaMnO}_{3-\delta}$ perovskite composites for aqueous organic pollutants decontamination, *Appl. Catal. B Environ.* 245 (2019) 546–554.
- [45] P. Zeng, Z. Chen, W. Zhou, H. Gu, Z. Shao, S. Liu, Re-evaluation of $\text{Ba}_{0.5}\text{Sr}_{0.5}\text{Co}_{0.8}\text{Fe}_{0.2}\text{O}_{3-\delta}$ perovskite as oxygen semi-permeable membrane, *J. Membr. Sci.* 291 (2007) 148–156.
- [46] J. Li, J. Miao, X. Duan, J. Dai, Q. Liu, S. Wang, W. Zhou, Z. Shao, Fine-tuning surface properties of perovskites via nanocompositing with inert oxide toward developing superior catalysts for advanced oxidation, *Adv. Funct. Mater.* 28 (2018), 1804654.
- [47] S. Sengodan, S. Ahn, J. Shin, G. Kim, Oxidation-reduction behavior of $\text{La}_{0.8}\text{Sr}_{0.2}\text{Sc}_y\text{Mn}_{1-y}\text{O}_{3\pm\delta}$ ($y=0.2, 0.3, 0.4$): Defect structure, thermodynamic and electrical properties, *Solid State Ion.* 228 (2012) 25–31.
- [48] S.B. Hammouda, F. Zhao, Z. Safaei, D.L. Ramasamy, B. Doshi, M. Sillanpää, Sulfate radical-mediated degradation and mineralization of bisphenol F in neutral medium by the novel magnetic $\text{Sr}_2\text{CoFeO}_6$ double perovskite oxide catalyzed peroxymonosulfate: Influence of co-existing chemicals and UV irradiation, *Appl. Catal. B Environ.* 233 (2018) 99–111.
- [49] J. Miao, J. Sunarso, C. Su, W. Zhou, S. Wang, Z. Shao, $\text{SrCo}_{1-x}\text{Ti}_x\text{O}_{3-\delta}$ perovskites as excellent catalysts for fast degradation of water contaminants in neutral and alkaline solutions, *Sci. Rep.* 7 (2017) 44215.
- [50] X. Duan, C. Su, J. Miao, Y. Zhong, Z. Shao, S. Wang, H. Sun, Insights into perovskite-catalyzed peroxymonosulfate activation: maneuverable cobalt sites for promoted evolution of sulfate radicals, *Appl. Catal. B Environ.* 220 (2018) 626–634.
- [51] Y. Pan, X. Xu, Y. Zhong, L. Ge, Y. Chen, J.-P.M. Veder, D. Guan, R. O'Hayre, M. Li, G. Wang, H. Wang, W. Zhou, Z. Shao, Direct evidence of boosted oxygen evolution over perovskite by enhanced lattice oxygen participation, *Nat. Commun.* 11 (2020) 2002.
- [52] J.T. Mefford, X. Rong, A.M. Abakumov, W.G. Hardin, S. Dai, A.M. Kolpak, K. P. Johnston, K.J. Stevenson, Water electrolysis on $\text{La}_{1-x}\text{Sr}_x\text{CoO}_{3-\delta}$ perovskite electrocatalysts, *Nat. Commun.* 7 (2016) 11053.